

Decoupled few-femtosecond phase transitions in vanadium dioxide

Christian Brahms^{1*}, Lin Zhang², Xiao Shen³, Utso Bhattacharya^{2,4}, Maria Recasens², Johann Osmond², Tobias Grass^{5,6}, Ravindra W. Chhajlany⁷, Kent A. Hallman⁸, Richard F. Haglund⁸, Sokrates T. Pantelides^{8,9}, Maciej Lewenstein^{2,10}, John C. Travers¹, and Allan S. Johnson^{11†}

¹School of Engineering and Physical Sciences, Heriot-Watt University, Edinburgh EH14 4AS, UK

²ICFO - Institut de Ciències Fotoniques, The Barcelona Institute of Science and Technology, Avenida Carl Friedrich Gauss 3, E-08860 Castelldefels (Barcelona), Spain

³Department of Physics and Materials Science, University of Memphis, Memphis, Tennessee 38152, USA

⁴Institute for Theoretical Physics, ETH Zurich, 8093 Zurich, Switzerland

⁵DIPC - Donostia International Physics Center, Paseo Manuel de Lardizabal 4, 20018 San Sebastian, Spain

⁶IKERBASQUE, Basque Foundation for Science, Plaza Euskadi 5, 48009 Bilbao, Spain

⁷Institute of Spintronics and Quantum Information, Faculty of Physics, Adam Mickiewicz University, 61-614 Poznań, Poland

⁸Department of Physics and Astronomy, Vanderbilt University, Nashville, Tennessee 37235, USA

⁹Department of Electrical and Computer Engineering, Vanderbilt University, Nashville, Tennessee 37235, USA

¹⁰ICREA, Passeig Lluís Companys 23, 08010 Barcelona, Spain

¹¹IMDEA Nanoscience, Calle Faraday 9, 28049, Madrid, Spain

*c.brahms@hw.ac.uk

†allan.johnson@imdea.org

The nature of the insulator-to-metal phase transition in vanadium dioxide (VO₂) is one of the longest-standing problems in condensed-matter physics^{1,2}. Ultrafast spectroscopy has long promised to determine whether the transition is primarily driven by the electronic or structural degree of freedom, but measurements to date have been stymied by their sensitivity to only one of these components and/or their limited temporal resolution³⁻⁶. Here we use ultra-broadband few-femtosecond pump-probe spectroscopy^{7,8} to resolve the electronic and structural phase transitions in VO₂ at their fundamental time scales. We find that the system transforms into a bad-metallic phase within 10 fs after photoexcitation, but requires another 100 fs to complete the transition, during which we observe electronic oscillations and a partial re-opening of the bandgap, signalling a transient semi-metallic state. Comparisons with tensor-network simulations and density-functional theory calculations show these features originate from oscillations around the equilibrium high-symmetry atomic positions during an unprecedentedly fast structural transition, in which the vanadium dimers separate and untwist with two different timescales. Our results resolve the complete structural and electronic nature of the light-induced phase transition in VO₂ and establish ultra-broadband few-femtosecond spectroscopy as a powerful new tool for studying quantum materials out of equilibrium.

Strong correlations between internal degrees of freedom create the extraordinary properties of quantum materials, but also make it challenging to identify which interactions underlie any specific phenomenon. The insulator-to-metal transition (IMT) in vanadium dioxide (VO₂) exemplifies this challenge^{1,2,9}: whether the IMT is primarily electronically or structurally driven has been debated for over 50 years. In the low-temperature monoclinic insulating (M1) phase of VO₂, the vanadium ions form pairs of twisted dimers (Fig. 1a). The vanadium 3d-orbitals form bands of $d_{||}$ and π^* symmetry (Fig. 1b) oriented along and away from the dimer chains, respectively (Fig 1c). The $d_{||}$ band splits into a filled bonding and an empty anti-bonding band, while the π^* bands lie above the Fermi energy, opening a bandgap. Upon heating above 340 K, both the band splitting and structural distortion disappear and VO₂ transitions to a metallic rutile (R) structure with evenly spaced vanadium ions and a single $d_{||}$ band at the Fermi level (Fig. 1a and b). However, whether a Peierls-like structural instability and crystal-field splitting of the $d_{||}$ band is sufficient to produce the bandgap has long

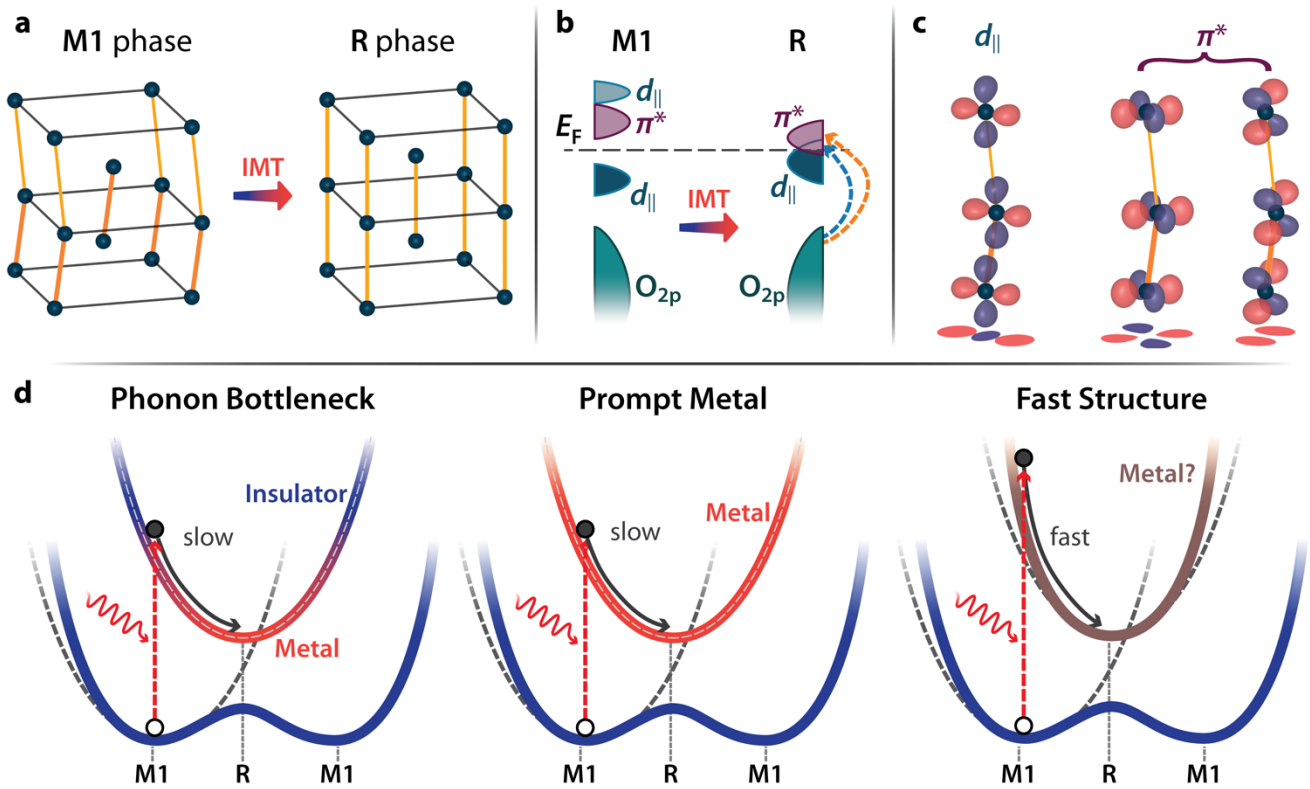


Fig. 1: The light-induced phase transition in VO₂. **a**, Structure of VO₂ in the monoclinic (M1) and rutile (R) phases. Oxygen atoms are omitted for clarity. **b**, Associated electronic changes between the phases. In the M1 phase, the d_{\parallel} band splits and the π^* orbitals move to higher energies, opening a bandgap. Also indicated are the main optical transitions in the R phase as determined by ellipsometry (see methods). **c**, Orbital structure of the two main bands involved in the IMT. The dimerisation and tilt in the M1 vanadium chains change the overlap of the d_{\parallel} orbitals and two π^* orbitals. **d**, Possible scenarios for the interplay of the structural and electronic components of the ultrafast IMT. Photoexcitation causes a sudden change of lattice potential. In the phonon bottleneck picture, VO₂ remains insulating until the structure transforms, while in the prompt metal scenario the system abruptly metallises and the structure transforms later. In the fast structural scenario, the lattice moves faster than the linear phonon modes, leaving it unclear if the structural transformation follows the electronic one or vice versa. Dashed lines show the harmonic approximation to the lattice potential.

been debated⁹. In another interpretation, VO₂ is a Mott insulator, so the d_{\parallel} band is split primarily by electron correlations, and the structural transition is secondary².

Ultrafast spectroscopy has been a key tool used to address this and similar questions, because it can decouple the normally concurrent changes in different degrees of freedom¹⁰. Intuitively, in a structurally driven IMT, the electronic system cannot metallise until the slow structural transition has occurred. An 80 fs “speed limit” in the electronic response in early experiments matched the period of the phonon modes connecting the M1 and R phases and was taken as evidence of a structurally driven transition³ (Fig. 1d, left). However, later experiments using attosecond extreme-ultraviolet and/or few-cycle infrared pulses^{5,6} observed transition times as low as 25 fs^{5,6}, far below the phonon period. These observations suggested a Mott-like transition, in which VO₂ metallises instantaneously while remaining structurally monoclinic and completes the transition to rutile later (Fig. 1d, middle). Because these experiments were predominantly sensitive to the electronic degree of freedom, their interpretations share the *a priori* assumption that the linear phonon modes of the M1 phase limit the speed of lattice motion^{3,5,6}. However, the vanadium dimers displace by ≈ 0.3 Å during the phase transition, well into the nonlinear phonon limit¹¹. This could lead to extremely rapid structural motion with or without simultaneous metallisation (Fig. 1d, right). Ultrafast diffraction measurements show that the structure transforms in 100 fs or less^{4,12,13}, but this is limited by the experimental time resolution. Therefore,

disentangling the two degrees of freedom requires measurements with high time resolution and simultaneous structural and electronic sensitivity.

Here, we study the photoinduced IMT in VO₂ via ultrafast optical spectroscopy with ~5 fs resolution and a probe spectrum spanning from the deep ultraviolet to the infrared, which we generate via soliton self-compression and resonant dispersive wave emission in gas-filled hollow capillary fibres^{7,8}. The ultra-broadband spectral window allows us to probe all valence and conduction band transitions simultaneously and observe the collapse of the bandgap, rise of the metallic Drude response, and evolution of the charge-transfer bands¹⁴. Tracking the full dielectric response guarantees sensitivity to structural changes, as the 1st-order coupling of light is not to free electrons but to their dipole with the nuclei. From this, we can build a complete picture of the changes in both the electronic and structural degrees of freedom with femtosecond time resolution. Where previous measurements observed a simple monotonic switching at this timescale^{5,6,12,15-17}, we find that the system follows a complex pathway. Within 10 fs after photoexcitation, the system is best described as a very bad metal^{14,18} with a Drude scattering time of only 0.1 fs. Surprisingly, this highly non-equilibrium state persists for over 100 fs. In parallel, the $d_{||}$ bands at the Fermi edge exhibit complex, 20 fs-scale changes which also decay over 100 fs. These results suggest that both the electronic configuration and the structure evolve extremely quickly after photoexcitation, with no speed limit imposed by the normal phonon modes. Our interpretation is supported by advanced electronic tensor network with self-consistent phononic mean field (TN-MF) calculations of a dimer chain, which show that the two structural distortions of the monoclinic phase disappear on different sub-50 fs timescales. Additional density-functional theory (DFT) calculations confirm that such a transient configuration is metallic and exhibits density-of-states bottlenecks which slow down hot-electron relaxation.

In our experiments, we induce the IMT in VO₂ with few-femtosecond pump pulses centred around 610 nm and probe the delay-dependent reflectivity of our sample with a sub-cycle-duration supercontinuum spanning 220 nm to 2550 nm⁸ (Methods and extended data Fig. S1). Figure 2a shows the experimentally measured delay-dependent differential reflectivity ($\Delta R/R$) of our 45 nm thick VO₂ film between 220 nm and 1130 nm at a pump fluence of 29 mJ/cm², sufficiently above the phase transition threshold of 10 mJ/cm² to ensure full transformation of the film (extended data Fig. S2). Three key features are evident: i) at temporal overlap (zero delay), the reflectivity changes very abruptly across the entire spectral window; ii) the subsequent evolution is complex with rapid changes; and iii) this initial evolution is completed within around 100 fs. This complex behaviour is in sharp contrast to previous studies of VO₂^{3,5,6,15,19,20}, and is revealed only via our improved temporal resolution and spectral bandwidth. To quantify the speed of the initial response, Fig. 2b shows kinetic traces in three wavelength bands indicated in Fig. 2a, along with fits to an initial step convolved with a double exponential decay. In all three bands, the response time is below 10 fs; in the ultraviolet it is below 5 fs. This response time is the fastest yet recorded in VO₂^{5,6} and suggests that this part of the transition is effectively instantaneous.

For a more detailed analysis, we leverage our ultra-broadband probe and extract the evolution of the Drude plasma and vanadium 3d bands. Using auxiliary static measurements, we convert $\Delta R/R$ at each time delay into an absolute reflectivity R . We then fit $R(\omega)$, where ω is photon energy, using the metallic rutile-phase permittivity, $\varepsilon(\omega) = \varepsilon'(\omega) + i\varepsilon''(\omega)$. We follow the model of ref. 21, in which the relevant transitions are those from the filled O_{2p} band to the empty vanadium $d_{||}$, π^* and σ^* bands, as well as the intraband Drude plasma (Methods). Figure 2d shows the resulting ε'' at 200 fs delay (black dashed) and relevant constituent transitions (coloured lines). Both the total response and the underlying components agree well with previous results^{14,21,22}. We can accurately describe the dynamics allowing only the $d_{||}$ and π^* bands and Drude term to vary (Methods), in good agreement with the general understanding of the IMT^{1,23}. Fig. 2c shows $\Delta R/R$ for the resulting fit and Figs. 2e-j the time evolution of the fit parameters. The grey shaded areas indicate negative delays, for which the sample is in the M1 phase. As the R-phase

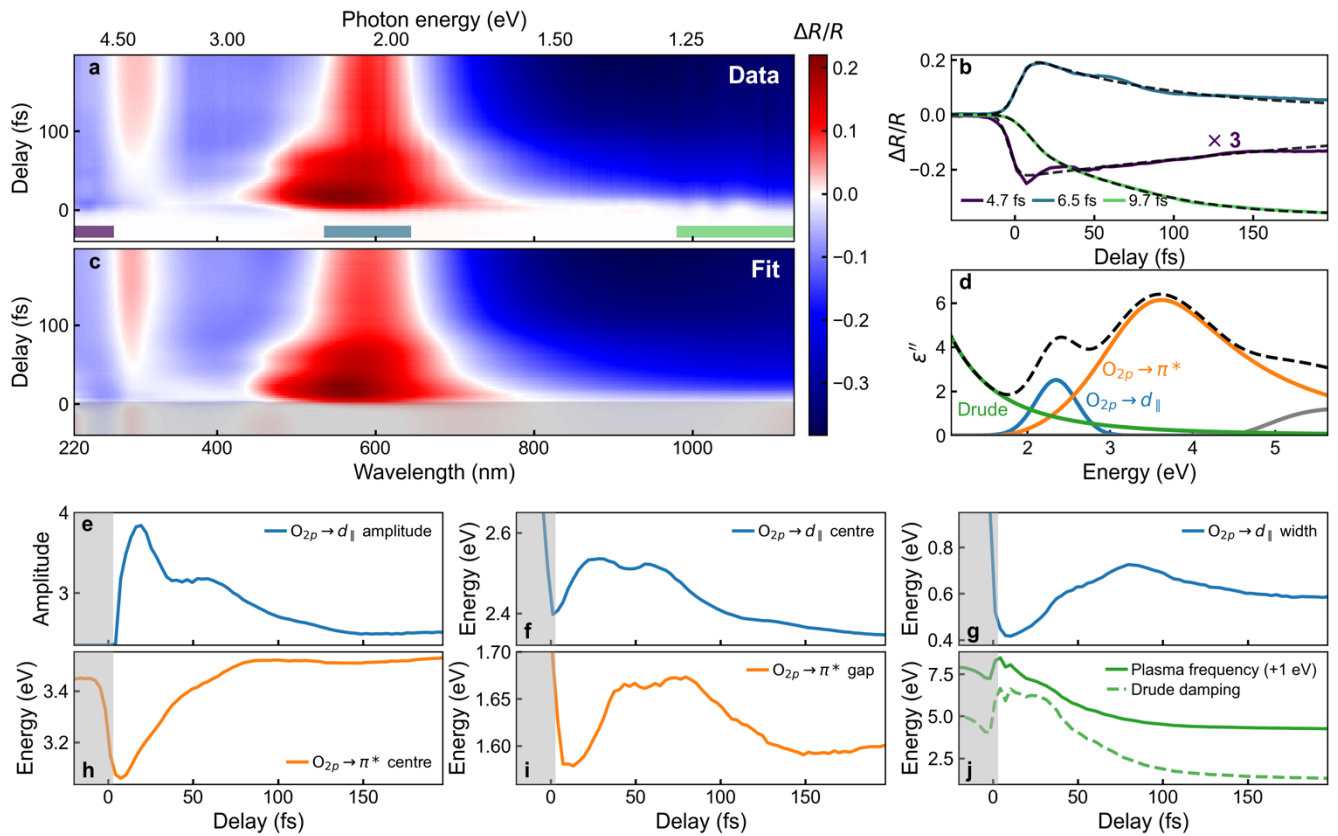


Fig. 2: Ultra-broadband ultrafast spectroscopy of the photoinduced phase transition in VO₂. **a**, Transient reflectivity of a 45 nm thick VO₂ thin film on sapphire when excited through the phase transition. A variety of non-trivial dynamics are seen at all regions of the spectrum. **b**, Lineouts and rise time fits of the dynamics averaged over wavelength in the three spectral bands indicated in panel **a**. Transition times as low as 5 fs (temporal resolution limited) are observed. **c**, Fit of the transient differential reflectivity using the metallic phase dielectric function. **d**, The dielectric function of the rutile metallic phase (dashed line), as well as the constituent resonances (solid). Only the Drude term and the two indicated optical transitions (coloured lines) are allowed to vary in fitting the experimental data in panel **a**. The $O_{2p} \rightarrow d_{||}$ resonance is modelled as a Gaussian while the $O_{2p} \rightarrow \pi^*$ is modelled as a Tauc-Lorentz resonator. **e-j**, Variation of the fitting parameters from panel **d** with pump-probe delay. All parameters of the Drude and $O_{2p} \rightarrow d_{||}$ transitions are allowed to vary freely, while for the $O_{2p} \rightarrow \pi^*$ resonance the width and amplitude are fixed. This set of parameters represents the minimal best fit to the data; further details on the fitting procedure and model in Methods.

dielectric function cannot describe this phase, the parameters in this region are spurious. For positive delays, the fit captures the data extremely well, indicating that the sample metallises immediately upon photoexcitation. After 100 fs the optical response closely resembles that of the thermal rutile phase and the evolution slows down significantly, in excellent agreement with the fastest directly structurally sensitive measurements^{4,12}.

We first focus on the Drude response (Fig. 2j). The free-carrier density is initially around 50% higher than in the thermal metallic phase and decays monotonically. The damping coefficient immediately after photoexcitation is 6.6 eV, which corresponds to an electron scattering time of only ≈ 0.1 fs and indicates very strong electron-electron interactions. This is extreme even for VO₂, which is known as a bad metal with scattering times below the Mott-Ioffe-Regel limit^{14,24}, and should lead to very fast relaxation. The ~ 100 -fs timescale thus implies a barrier to electron-hole recombination.

We next consider the dynamics of the vanadium 3d bands (Figs. 2e-j). Because the O_{2p} orbitals exhibit only marginal changes during the IMT²³, the $O_{2p} \rightarrow d_{||}$ and $O_{2p} \rightarrow \pi^*$ transitions effectively track the motion of the unoccupied portion of the $d_{||}$ and π^* bands above the Fermi level. The $O_{2p} \rightarrow d_{||}$ and $O_{2p} \rightarrow \pi^*$ transitions are fit via a Gaussian and Tauc-Lorentz respectively²¹. There are clear double-peak revival structures on a 20-fs timescale, most obvious in

the amplitude and central energy of the $d_{||}$ transition (Figs. 2e and f). Similar structures can be seen in Figs. 2g and i. This motion cannot result from coherent electronic effects as it is much slower than the scattering times for conduction-band electrons. Conversely, it is faster than the phonon modes previously considered to govern the phase transition^{3,25,26}. As shown in Figure 2h, the π^* band energy moves monotonically over a similar timescale to the Drude response, while the dynamics of the gap term shown in Figure 2i agree qualitatively with those of the $d_{||}$ band. This shows internal consistency of the fits, as the gap term in a Tauc-Lorentz model is related to the next-lowest-lying band²⁷.

The motion of the $d_{||}$ and π^* transitions leads us to a surprising conclusion even before considering its origin. The $O_{2p} \rightarrow d_{||}$ transition promotes electrons to just above the Fermi level (see Fig. 1b). After less than 10 fs, it has a central energy of 2.4 eV and bandwidth of 0.4 eV (Fig. 2f and g), very close to equilibrium metal values (2.35 eV and 0.6 eV, respectively). This shows that the $d_{||}$ -band splitting collapses quasi-instantaneously, in good agreement with the rapid metallisation. However, after 30 fs the $d_{||}$ transition has moved upward to 2.55 eV with 0.45 eV bandwidth (Fig. 2f and g). This shift and broadening indicate a reduced density of states (DOS) at the Fermi level (see Extended Data Fig. S3). In particular, the central-energy change closely matches the 0.2 eV shift of the unoccupied bands during the thermal IMT²³. Our data thus suggests that within 30 fs, the direct band gap partially re-opens and VO₂ becomes transiently semimetallic. This explains the slow relaxation of the Drude plasma: while intraband collisions are extremely frequent, a transient DOS bottleneck near the Fermi level limits electron-hole recombination until the $d_{||}$ states have completely relaxed, which takes around 100 fs²⁸. We note the reduced width of the $d_{||}$ band as compared to the thermal R-phase is also a plausible explanation for the increased intraband scattering rate.

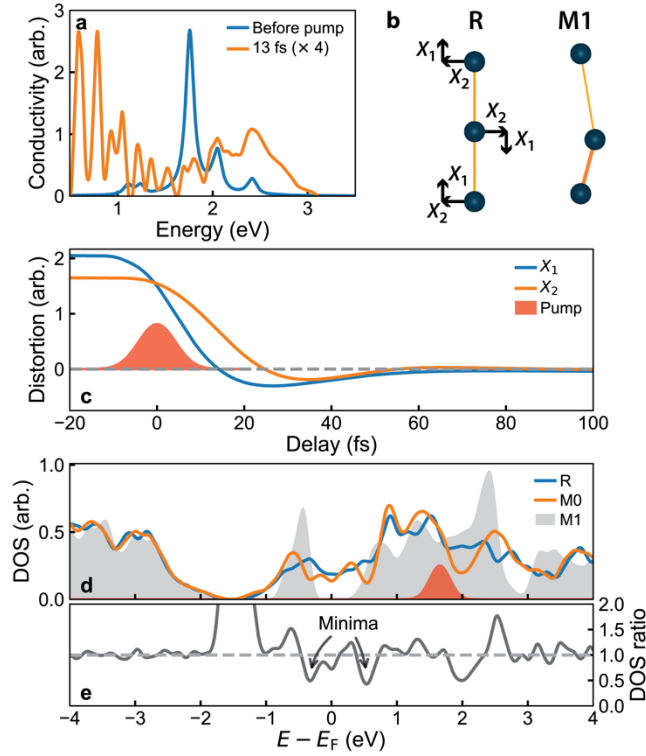


Figure 3: Simulations of the ultrafast phase transition. **a**, TN-MF simulated optical conductivity before and 13 fs after photoexcitation showing instantaneous bandgap collapse. **b**, Illustration of the two components of the structural distortion. **c**, Structural dynamics following the phase transition. The dimerization relaxes prior to the tilt, overshooting the rutile positions, before fully relaxing in less than 100 fs. **d**, DOS calculated with DFT for the monoclinic and rutile phases, and for a structural configuration (M0) close to that predicted by the TN-MF calculations for ~ 20 fs delay. **e**, Ratio of the DOS of the M0 configuration and the rutile phase. The DOS near the Fermi level in the M0 phase exhibits several minima as compared to the rutile phase. Electrons generated at energies excited by the pump (red Gaussian in **d**) need to relax across these minima prior to full thermalization.

To understand the dynamics of the d_{\parallel} and π^* bands, we have performed calculations of the light-induced phase transition using a TN-MF approach²⁹. Motivated by the dominance of the d_{\parallel} and π^* bands, we model a two-band system and solve the fully quantum equations of motion for the electronic degree of freedom. We treat the nuclei classically and model the dimerisation and tilt as two independent components in a sixth-order Landau potential to describe the 1st-order nature of the phase transition⁹. We validate this approach by recovering the thermal phase transition using finite-temperature tensor-network calculations and describe photoexcitation with a Peierls substitution; further details in the methods section and Ref. 29.

Figure 3 shows the results of these simulations. In agreement with experiment, we find a prompt collapse of the bandgap in the optical conductivity after only 13 fs (Fig. 3a). More surprisingly, the two components of the structural distortion (Fig. 3b) transform in just tens of femtoseconds (Fig. 3c), faster than the linear phonon modes of the system and in agreement with the timescales for motion of the d_{\parallel} and π^* transitions observed in experiment. In the simulations, the displacement of the dimers (X_1) is lost faster than the tilt (X_2)—similar to early proposals about the structural transformation in VO_2 ²⁵, but several orders of magnitude faster. The high velocity results in significant inertia, whereby the displacement undergoes a transient revival with opposite sign¹⁷. Similar effects have been predicted in recent time-dependent DFT calculations³⁰, though here we find no strong dependence on the photocarrier doping level, in agreement with recent diffraction measurements³¹.

These findings are in excellent agreement with our experimental data and provide a plausible explanation for the complex evolution of the electronic state. The d_{\parallel} band is strongly sensitive to both displacement and tilt of the dimers

as they affect the overlap of the orbitals along the dimerization direction. The oscillations in the $d_{||}$ band can then be explained as due to (a) the loss and subsequent partial restoration of the displacement leading to an oscillation of the orbital overlap and (b) the separate timescale for the evolution of the tilt. Conversely, the π^* orbitals are aligned perpendicular to the dimer chains and hence less sensitive to the displacement. This band is governed either by tilt, which disappears more slowly and monotonically, or by the relaxation of carriers.

To further verify that the band dynamics can be explained by structural changes, we have compared our results to electronic structures calculated using DFT based on a hybrid exchange functional (see Methods). In particular, the TN-MF dynamical calculations predict that the system passes through a metallic phase with greatly reduced dimerization and tilt as compared to the M1 phase. This state is similar to the recently proposed M0 phase³². In Figure 3d and e we compare the DOS calculated for the M1, M0 and R phases using this approach (Methods). A single hybrid exchange functional is used to describe all three phases, making it uniquely suited to examine out-of-equilibrium states. Compared to the R phase, the M0-phase DOS shows several minima near the Fermi level (-0.4 eV to 0.6 eV) and changes from predominantly π^* character to predominantly $d_{||}$ in this region. As our 2 eV pump pulse primarily excites $d_{||} \rightarrow \pi^*$ transitions in the M1 phase²¹, the photoexcited carriers are initially centred at an energy of 1.5 eV, as indicated by the red Gaussian in Fig. 3c. This feature supports our interpretation of the experimental data: the hot carriers have to relax across DOS bottlenecks, so the non-equilibrium state can persist for much longer than would be expected.

We can now provide a comprehensive description of the light-induced IMT in VO₂ at the shortest timescales, as schematically illustrated in Figure 4. Photoexcitation causes a purely electronic collapse of the bandgap and transition to a monoclinic metallic state within 10 fs. This metallic state is characterized at first by extremely bad metallicity^{14,24}, and then by semi-metallicity caused by the competing crystal-field splitting that favours re-opening the bandgap¹. The fast electronic rearrangement creates a large, non-adiabatic force on the vanadium ions. In response, the ions move towards their rutile positions faster than the characteristic phonon frequencies of the monoclinic phase. As the structure relaxes, the crystal-field splitting of the conduction band reduces, but structural overshoots due to the large ion inertia can transiently revive this feature. After just 100 fs, the structure fully relaxes due to the strong electron-

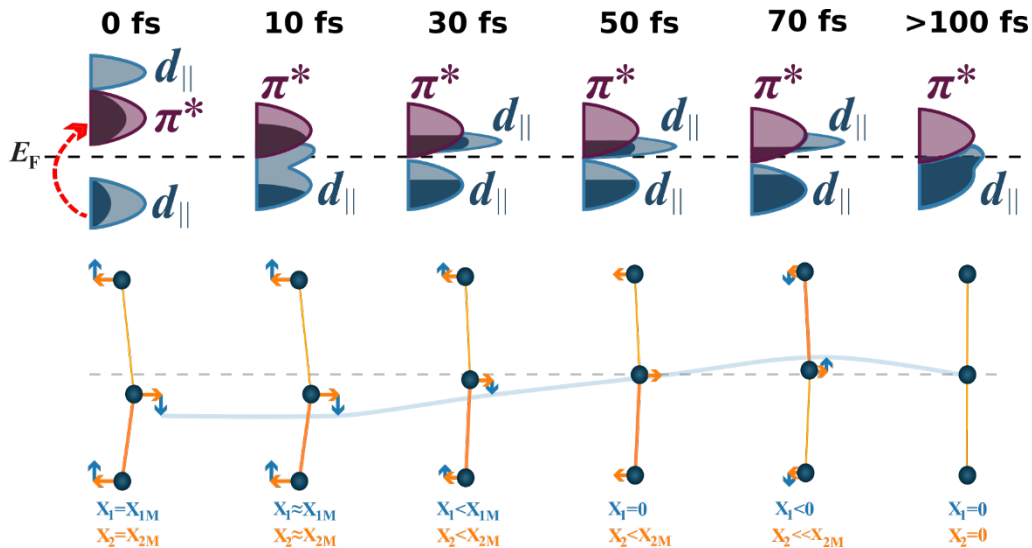


Figure 4: Electronic and structural changes during the light-induced IMT of VO₂. The system begins in the M1 phase, then photoexcitation causes a prompt electronic phase transition and the bandgap collapses. This launches rapid and coherent phonon motion, causing the lattice to transform faster than would be expected from the normal phonon modes. The structural competition/electron cooling causes the electronic structure to partially re-open the bandgap as the dimerization and tilt coherently evolve, stymying further purely electronic relaxation. After 100 fs strong electron-phonon scatters cools the electrons and heats the lattice, damping all coherent motion, and the system approaches the thermal rutile phase.

lattice coupling⁴ and the system approaches the thermal metallic state, with strain- and temperature-propagation effects occurring on longer timescales¹⁶.

Our new experimental and theoretical methods reveal the surprising complexity of the early-time dynamics of the light-induced phase transition in VO₂. In equilibrium, a cooperative effect between Mott-like electronic interactions and crystal-field splitting has been suggested to explain the bandgap in the monoclinic phase^{9,33}. Here, we find that these effects can be competitive when out of equilibrium, and that the quasi-instantaneous electronic re-arrangement can trigger non-linear lattice dynamics. Because the electronic structure transforms prior to structural rearrangement, the system transiently passes through a monoclinic metallic state. This suggests it should be possible to drive an electronic-only phase transition, in qualitative agreement with a Mott picture^{5,6}. However, our results also indicate that any such phase would be very short-lived: the strong electron-phonon coupling would transfer energy to the lattice bath in less than 100 fs⁴, so the system would revert to the insulating state unless sufficient energy is provided to also trigger the structural transformation. Any monoclinic-phase metal that does not subsequently transform to the rutile phase would, therefore, likely be found in a narrow fluence range just below the transition threshold and have a lifetime of at most a few hundred femtoseconds. Our results also demonstrate the power of ultra-broadband, few-femtosecond spectroscopy enabled by soliton self-compression and resonant dispersive wave emission^{7,8} for understanding dynamics in the condensed phase. By directly tracking all relevant optical transitions for band-structure changes, we can build a comprehensive picture of the phase transition at short time scales which are inaccessible with other techniques. This methodology will find future applications in understanding other light-driven quantum materials³⁴ where broad resonances and multiple energy scales can challenge conventional methodologies, as well as enabling optical attosecond spectroscopy in the condensed phase⁸.

Methods

Sample Deposition and Characterization

An approximately 45 nm thick thin film of VO₂ was deposited onto a 001 (c-cut) sapphire substrate using pulsed laser deposition at room temperature and subsequent annealing³⁵. The mean-square strain was measured using the Williamson-Hall method to be 0.13, consistent with an earlier determination for a similar film. The dielectric properties and thickness were determined using ellipsometry. Data were taken at three angles of incidence (60, 65, and 70 degrees) and wavelengths spanning from 200 to 2700 nm, which were then fit with a similar model to that proposed in Qazilbash *et al.*²¹, yielding good agreement with the parameters determined there. A film thickness of 45 nm and a penetration depth of 65 nm at 660 nm wavelength were determined. Upon heating above 340K a sharp change in the optical properties was observed as the sample underwent the phase transition in the rutile metallic phase. The full reflectivity of the rutile metallic phase was then fit to the same dielectric functions as in Qazilbash *et al.*²¹, with excellent agreement found in the dielectric parameters as compared to previous literature. In particular the imaginary part of the dielectric function was modelled as:

$$\varepsilon'' = \frac{A_{UV}}{\omega_{UV} - \omega} + \frac{A_{IR}}{\omega} + \text{Im} \left\{ G(\omega, A_{d_{||}}, \omega_{d_{||}}, \sigma_{d_{||}}) + TL(\omega, A_{\pi^*}, \omega_{\pi^*}, \sigma_{\pi^*}, g_{\pi^*}) + TL(\omega, A_{\sigma^*}, \omega_{\sigma^*}, \sigma_{\sigma^*}, g_{\sigma^*}) - \frac{\omega_p^2}{\omega^2 + i\gamma\omega} \right\},$$

where ω is the photon energy, G denotes a causality-corrected Gaussian function³⁶ and TL denotes a Tauc-Lorentz function²⁷; the real part is related via the Kramers-Kronig relations. The terms in the expression are a UV pole, IR pole, Gaussian resonance describing the O_{2p} → d_{||} transition, a Tauc-Lorentz describing the O_{2p} → π* transition, a Tauc-Lorentz describing the O_{2p} → σ* transition, and the Drude plasma term. The Drude plasma term is determined by the plasma frequency ω_p and damping term γ . Apart from the Drude term, in each case A_X , ω_X , and σ_X denote the amplitude, resonant frequency and width of resonance X. The Tauc-Lorentz resonances include an additional term g_X which denotes the “gap” term. In a semiconductor or insulator the gap term denotes the energy of the bandgap; for

photon energies below this, the probability of the optical transition goes to zero, leading to a strong asymmetry in the resonance structure. In materials without a bandgap there is no sharp “turn on” energy to the resonance, and this term instead relates approximately to the next lowest lying energy band into which carriers can be promoted instead of to the Tauc-Lorentz resonance, leading to a more gradual “turn on” of the resonance.

Ultrafast Spectroscopy

A schematic of the experimental apparatus for ultra-broadband few-femtosecond spectroscopy is shown extended data Fig. S4. A titanium-doped sapphire amplifier (Coherent Legend Elite Duo USP) delivers 35 fs pulses (full width at half-maximum, FWHM) with 8 mJ of energy at 1 kHz repetition rate. These are converted to 1.45 mJ pulses at 1750 nm in an optical parametric amplifier (Light Conversion TOPAS-PRIME-HE). The infrared pulses are spectrally broadened in a gas-filled hollow capillary fibre (HCF) with 700 μm core diameter and 1.25 m length which is filled with argon gas at 450 mbar pressure, and subsequently compressed by propagation through bulk material. This results in 12 fs FWHM pulses with around 1 mJ of energy. A beamsplitter divides the beam into two, and both beams pass through variable attenuators formed of an achromatic half-wave plate and a silicon plate at Brewster’s angle before being coupled into separate HCFs for the generation of pump and probe pulses.

The pump pulse is generated via soliton self-compression and resonant dispersive wave (RDW) emission in a 1.3 m HCF with 450 μm core diameter filled with 1050 mbar of argon. When driving this HCF with around 135 μJ of pulse energy (measured before the HCF entrance window), around 22 μJ of energy is converted into an RDW pulse centred at 610 nm with a transform-limited pulse duration of approximately 3.5 fs. After exiting the HCF system this pulse passes through a 0.5 mm CaF_2 beam sampler and a motorised chopper wheel and then into the vacuum chamber. After collimation with a spherical metallic mirror, four chirped mirrors (Ultrafast Innovations PC70) both compensate for the dispersion of optical components and act as dichroic mirrors to remove the infrared supercontinuum from the pump beam. An in-vacuum half-wave plate and silicon-plate form an attenuator for the pump pulse. The filtered and attenuated pulse is then focused onto the VO_2 sample with a spherical metallic mirror to a spot size of approximately 200 μm FWHM.

A second HCF with 200 μm core diameter and 40 cm length provides the probe pulses. This HCF is directly connected to the vacuum chamber, creating a pressure gradient; the argon pressure in the entrance cell is maintained at 800 mbar with an electronic flow regulator. With 150 μJ of driving energy (measured before the HCF entrance window), a supercontinuum spanning 220 nm to 2550 nm is generated by extreme soliton self-compression. After collimation with a spherical mirror with a UV-enhanced aluminium coating, the probe beam is attenuated by reflection from two wedged glass windows before being refocused to a spot size of approximately 38 μm FWHM on the sample. The reflected probe beam is then reimaged with 6x magnification onto the 25 μm entrance slit of a CCD spectrometer (Avantes ULS2048XL, detection range 200-1160 nm with 1715 pixels) outside the vacuum chamber by another spherical mirror, thus sampling only the central region of the probe. A half-wave plate before the probe generation HCF rotates the probe polarisation to be opposite to that of the pump; a polariser just before the spectrometer thus passes the probe but suppresses scatter from the pump.

Pump-probe measurements are acquired in a single-shot pump-on/pump-off scheme. The chopper wheel is synchronised to switch the pump pulse at half the laser repetition rate. The pump-probe delay is scanned in steps of 1 fs by a motorised delay stage in the probe arm. 2000 probe shots are acquired at each delay (with the pump on for half of these).

We calculate the differential reflectivity as $\Delta R/R = (I_{\text{on}} - I_{\text{off}})/I_{\text{off}}$, where I_{on} and I_{off} are the spectra with the pump on and off, respectively. To reduce the effect of detector noise, we average all spectra in five-pixel bins along the wavelength axis, resulting in wavelength samples separated by approximately 3 nm. Because of minor alignment drifts

between pump-probe scans, we numerically correct the delay axis of each scan by overlapping the fastest delay-dependent feature in our data (see extended data Fig. S5). To remove fast oscillations caused by interference with residual pump scatter, we then re-bin along the delay axis, resulting in a spacing of 3 fs between delay points. Beyond removing the fast oscillations this does not affect the observed dynamics (see extended data Fig. S6). We then further de-noise the data through a principal-component analysis (see extended data Fig. S7). We retain the four most significant components, which captures all the salient features in our experimental data.

Dynamics Fitting

The differential reflectivity reported in Figure 2a is first converted into an absolute reflectivity using the reflectivity of the M1 phase extracted from ellipsometry. The reflectivity at each time step as a function of probe photon energy is then fit using the dielectric function of the rutile metallic phase; we begin by fitting the long time delays (200 fs) at which the reflectivity agrees well with the thermal metallic state, and then move backwards in pump-probe delay, updating our initial guess with the output from the previous time delay. The full dielectric function has 14 free parameters and clearly overfits the data. Instead, we systematically fix a number of parameters to agree with the rutile metallic phase values and then allow the remaining parameters to vary freely. We examine all permutations of this fitting procedure (1969 combinations). The seven parameters shown in Figure 2c are found to be the optimal minimal set which can accurately describe the phase transition for the following reasons: (1) they are the set that minimizes the error when allowing seven parameters to vary. (2) When allowing fewer parameters to vary, the optimal parameters are always from this set of seven parameters. (3) They show self-consistency, particularly in the dynamics of the Tauc-Lorentz gap term (Figure 2i) and the Gaussian transition (Figure 2f,g), in which the gap term should be expected to track the edge of the next lowest transition. (4) Adding additional parameters induces unphysical behaviour in the time-behaviour, namely sudden jumps. (5) Qualitatively, they are the minimal set which reproduces all salient features of the data after 20 fs delay. Additional parameters do not introduce improvements discernible by eye. (6) They are physically motivated by the known physics of the system as they relate exclusively to the π^* , d_{\parallel} and Drude terms which are known to exhibit the largest changes through the phase transition.

Time-dependent simulations of a dimer chain

These calculations are fully described in Zhang *et al.*²⁹. We consider the d_{\parallel} singlet and one π^* orbital to simplify the theoretical model without losing the important physics of VO₂. Since the Peierls instability mainly occurs in the c_R axis, we model VO₂ as a quasi-one-dimensional system, for which the displacement $\mathbf{X} \equiv (X_1, X_2)$ is introduced to capture the dimerizing displacement along c_R axis and the band-splitting displacement in the perpendicular plane, respectively. The total Hamiltonian is given by

$$H = H_e + H_{e-X} + \Phi(\mathbf{X}).$$

Here the pure electronic part reads

$$H_e = - \sum_i \sum_{a=1,2} \sum_{\sigma=\uparrow,\downarrow} t_a c_{a,\sigma,i}^\dagger c_{a,\sigma,i+1} - t_{12} \sum_i \sum_{\sigma=\uparrow,\downarrow} c_{1,\sigma,i}^\dagger c_{2,\sigma,i} + \text{H.c.} + \sum_i \sum_{a=1,2} \varepsilon_a n_{a,i} + \frac{U}{2} \sum_i n_i (n_i - 1),$$

where $a = 1,2$ denotes the d_{\parallel} and π^* orbital, respectively, t_a is the nearest-neighbour intra-orbital hopping, t_{12} is the onsite inter-orbital hopping, and ε_a is the onsite energy potential. We have

$$n_{a,i} = \sum_{\sigma=\uparrow,\downarrow} n_{a,\sigma,i},$$

$$n_i = \sum_{a=1,2} \sum_{\sigma=\uparrow,\downarrow} n_{a,\sigma,i},$$

and U is the onsite Hubbard repulsive interaction. The lattice distortion is modelled through the classical potential energy⁹

$$\Phi(X) = L \left[\frac{\alpha}{2} (X_1^2 + X_2^2) + \frac{\beta_1}{4} (2X_1 X_2)^2 + \frac{\beta_2}{4} (X_1^2 - X_2^2)^2 + \frac{\gamma}{6} (X_1^2 + X_2^2)^3 \right],$$

which is obtained from the Landau functional for improper ferroelectrics expanded up to the sixth order in the lattice displacements. Here L is the number of lattice sites. For the electron-lattice coupling, we have

$$H_{e-X} = -gX_1 \sum_i (-1)^i n_{1,i} - \frac{\delta}{2} X_2^2 \sum_i (n_{1,i} - n_{2,i}),$$

where the first term with coupling constant g describes the dimerization induced by the displacement X_1 along c_R axis while the second term with strength δ represents the crystal field splitting generated by X_2 . Here we take the half-bandwidth as the unit of energy and set $t_1 = t_2 = 0.5$ eV. The inter-orbital hopping is chosen as $t_{12} = 0.1$ eV. We also assume the centre of gravity for these two bands to be the same and set $\varepsilon_1 = \varepsilon_2 = 0$. The Hubbard interaction is $U = 0.6$ eV, and the parameters for the lattice potential are set as $\alpha = 0.155$ eV, $\beta_1 = 1.75 \times 10^{-3}$ eV, $\beta_2 = 2\beta_1$, and $\gamma = 6.722 \times 10^{-4}$ eV. Finally, we choose the electron-lattice coupling strength as $g = 0.528$ eV and $\delta = 0.2$ eV, such that the transition temperature from the M1 phase to the R phase is close to the experimental value. The total system is at quarter filling. Under this coupling parameter convention X_1 and X_2 are dimensionless²⁹.

Simulation of the time evolution

We use the tensor network methods to simulate the time evolution of the system induced by light pulse, which couples to the electronic degrees of freedom through the Peierls substitution $t_\alpha \rightarrow t_\alpha e^{i\frac{e}{\hbar} A_{\text{pump}}(t)}$. Here $A_{\text{pump}}(t)$ is the vector potential for electric field $E_{\text{pump}}(t) = E_{0,\text{pump}} e^{-(t-t_{0,\text{pump}})^2/2\sigma_{\text{pump}}^2} \cos[\omega_{\text{pump}}(t - t_{0,\text{pump}})]$. We start from the equilibrium M1 phase at zero temperature with $X_1 \approx 2.05$ and $X_2 \approx 1.65$, which minimizes the internal energy $\Phi_{\text{eff}} = \Phi(X) + \langle H_{e-X} \rangle + \langle H_e \rangle$. The time evolution of the system is decomposed into two parts, i.e., the electronic and lattice degrees of freedom. For the evolution of electronic state $|\psi\rangle$, we use the Born-Oppenheimer approximation within each time step δt , i.e., the lattice distortions are approximated as fixed, while the electronic degrees of freedom are dynamic. The corresponding equation of motion is given by the Schrödinger equation and can be written as

$$|\psi(t + \delta t)\rangle = e^{-iH[t,X(t)]\delta t/\hbar} |\psi(t)\rangle,$$

which can be simulated by the infinite time-evolving block decimation method. On the other hand, we use the classical approximation for the lattice dynamics and invoke the Ehrenfest theorem for the motion of lattice degrees of freedom

$$M \frac{d^2 X_i}{dt^2} = F_i(t) - \xi \frac{dX_i}{dt},$$

where M is the effective mass of ions, which is set as 25 in this work, and ξ is the damping coefficient. The forces F_i are obtained through the Hellmann-Feynman theorem and explicitly read

$$F_1 = \frac{g}{2} \sum_{i=1,2} \cos(Qi) \langle \psi | n_{1,i} | \psi \rangle - \alpha X_1 - 2\beta_1 X_1 X_2^2 - \beta_2 X_1 (X_1^2 - X_2^2) - \gamma X_1 (X_1^2 + X_2^2)^2$$

and

$$F_2 = \frac{\delta}{2} X_2 \sum_{i=1,2} \langle \psi | (n_{1,i} - n_{2,i}) | \psi \rangle - \alpha X_2 - 2\beta_1 X_1^2 X_2 + \beta_2 X_2 (X_1^2 - X_2^2) - \gamma X_2 (X_1^2 + X_2^2).$$

Time-dependent optical conductivity

Given the knowledge of the electronic wave function $|\psi(t)\rangle$ under the action of an external field $A(t)$, the temporal evolution of the current, defined as

$$\langle J(t) \rangle = \langle \psi(t) | J(t) | \psi(t) \rangle$$

with

$$J(t) = \frac{\delta H(t)}{\delta A(t)} = -i \sum_{a,\sigma,i} t_a \left[e^{i\frac{e}{\hbar} A(t)} c_{a,\sigma,i}^\dagger c_{a,\sigma,i+1} - \text{H.c.} \right],$$

can be readily obtained. To calculate the optical conductivity for a nonequilibrium system induced by the pump pulse, we employ the pump-probe based method proposed in Ref. ³⁷, where the temporal evolution of the system is traced twice in order to identify the response of the system with respect to the later probe pulse. The procedures are as follows. First, the time-evolution process induced by the pump pulse $A_{\text{pump}}(t)$ in the absence of probe pulse is evaluated, which describes the nonequilibrium development of the system, and we obtain the current $\langle J_{\text{pump}}(t) \rangle$. Second, in addition to the pump pulse, we also introduce a narrow probe pulse $A_{\text{probe}}(t)$ centered at time t_* , which leads to the current $\langle J_{\text{total}}(t) \rangle$. The subtraction of $\langle J_{\text{pump}}(t) \rangle$ from $\langle J_{\text{total}}(t) \rangle$ produces the variation of the current due to the presence of probe pulse, i.e., $\langle J_{\text{probe}}(t) \rangle$, with which the time-dependent optical conductivity at time t_* can be calculated through

$$\sigma(\omega) = \frac{J_{\text{probe}}(\omega)}{i(\omega + i\eta) L A_{\text{probe}}(\omega)},$$

where $J_{\text{probe}}(\omega)$ and $A_{\text{probe}}(\omega)$ are the Fourier transformation of $\langle J_{\text{probe}}(t) \rangle$ and $A_{\text{probe}}(t)$, respectively. Numerically, a damping factor $e^{-\eta t}$ shall be introduced in the Fourier transformations, and the same η is included in the denominator of the above equation.

Density functional theory simulations

The DFT calculations were carried out using a plane-wave basis. We use the projector-augmented wave method³⁸, which is implemented in the Vienna Ab initio Simulation Package (VASP)³⁹. The exchange and correlation were described using a tuned PBE0 hybrid functional^{40,41} with 7% Hartree-Fock exchange, same as Ref.³². For the vanadium pseudopotential, 13 electrons ($3s^2 3p^6 3d^3 4s^2$) were treated as valence electrons. For the oxygen pseudopotential, six electrons ($2s^2 2p^4$) were treated as valence electrons. The cutoff energy of the plane-wave was 400 eV. For structural optimizations, we used a Γ -centered $3 \times 3 \times 3$ grid for the M1 and M0 phases (12 atoms per unit cell) and a $4 \times 4 \times 6$ grid for the R phase (six atoms per unit cell). The electronic self-consistent calculations were converged to 10^{-4} eV between successive iterations, and the structural relaxations were converged to 10^{-3} eV between two successive ionic steps. The densities of states were calculated using a Γ -centered $7 \times 9 \times 7$ grid for the M1 and M0 phase and a Γ -

centered $9 \times 9 \times 15$ grid for the R phase. The crystal structures of the M1, M0 and R phases are shown in extended data Figure S8.

Data availability

Source data and plotting routines which reproduce all plots in Figs. 2 and 3 and extended data Figs. S1, S2, S3, and S5-S7 can be found at <https://doi.org/10.5281/zenodo.10617311>.

References

1. Goodenough, J. B. The two components of the crystallographic transition in VO₂. *Journal of Solid State Chemistry* **3**, 490–500 (1971).
2. Zylbersztein, A. & Mott, N. F. Metal-insulator transition in vanadium dioxide. *Phys. Rev. B* **11**, 4383–4395 (1975).
3. Cavalleri, A., Dekorsy, T., Chong, H. H. W., Kieffer, J. C. & Schoenlein, R. W. Evidence for a structurally-driven insulator-to-metal transition in VO₂: A view from the ultrafast timescale. *Physical Review B* **70**, 161102(R) (2004).
4. De La Peña Muñoz, G. A. *et al.* Ultrafast lattice disordering can be accelerated by electronic collisional forces. *Nat. Phys.* **19**, 1489–1494 (2023).
5. Bionta, M. R. *et al.* Probing the phase transition in VO₂ using few-cycle 1.8 μm pulses. *Phys. Rev. B* **97**, 125126 (2018).
6. Jager, M. F. *et al.* Tracking the insulator-to-metal phase transition in VO₂ with few-femtosecond extreme UV transient absorption spectroscopy. *Proceedings of the National Academy of Sciences* **114**, 9558–9563 (2017).
7. Travers, J. C., Grigorova, T. F., Brahms, C. & Belli, F. High-energy pulse self-compression and ultraviolet generation through soliton dynamics in hollow capillary fibres. *Nat. Photonics* **13**, 547–554 (2019).
8. Brahms, C., Belli, F. & Travers, J. C. Infrared attosecond field transients and UV to IR few-femtosecond pulses generated by high-energy soliton self-compression. *Physical Review Research* **2**, 043037 (2020).
9. Grandi, F., Amaricci, A. & Fabrizio, M. Unraveling the Mott-Peierls intrigue in vanadium dioxide. *Phys. Rev. Research* **2**, 013298 (2020).
10. Allen, P. B. Theory of thermal relaxation of electrons in metals. *Physical Review Letters* **59**, 1460–1463 (1987).
11. Von Hoegen, A., Mankowsky, R., Fechner, M., Först, M. & Cavalleri, A. Probing the interatomic potential of solids with strong-field nonlinear phononics. *Nature* **555**, 79–82 (2018).
12. Wall, S. *et al.* Ultrafast disordering of vanadium dimers in photoexcited VO₂. *Science* **362**, 572–576 (2018).
13. Xu, C. *et al.* Transient dynamics of the phase transition in VO₂ revealed by mega-electron-volt ultrafast electron diffraction. *Nat Commun* **14**, 1265 (2023).
14. Qazilbash, M. M. *et al.* Correlated metallic state of vanadium dioxide. *Physical Review B - Condensed Matter and Materials Physics* **74**, 205118 (2006).
15. Wall, S. *et al.* Ultrafast changes in lattice symmetry probed by coherent phonons. *Nature Communications* **3**, 721 (2012).
16. Johnson, A. S. *et al.* Ultrafast X-ray imaging of the light-induced phase transition in VO₂. *Nature Physics* **19**, 215–220 (2023).
17. Pashkin, A. *et al.* Ultrafast insulator-metal phase transition in VO₂ studied by multiterahertz spectroscopy. *Phys. Rev. B* **83**, 195120 (2011).
18. Phillips, P. W., Hussey, N. E. & Abbamonte, P. Stranger than metals. *Science* **377**, eabh4273 (2022).
19. Wegkamp, D. *et al.* Instantaneous band gap collapse in photoexcited monoclinic VO₂ due to photocarrier doping. *Physical Review Letters* **113**, 216401 (2014).
20. O’Callahan, B. T. *et al.* Inhomogeneity of the ultrafast insulator-to-metal transition dynamics of VO₂. *Nature Communications* **6**, 6849 (2015).
21. Qazilbash, M. M. *et al.* Electrodynamics of the vanadium oxides VO₂ and V₂O₃. *Physical Review B - Condensed Matter and Materials Physics* **77**, 115121 (2008).
22. Okazaki, K., Sugai, S., Muraoka, Y. & Hiroi, Z. Role of electron-electron and electron-phonon interaction effects in the optical conductivity of VO₂. *Phys. Rev. B* **73**, 165116 (2006).
23. Koethe, T. C. *et al.* Transfer of spectral weight and symmetry across the metal-insulator transition in VO₂. *Physical Review Letters* **97**, 116402 (2006).
24. Qazilbash, M. M. *et al.* Mott Transition in VO₂ Revealed by Infrared Spectroscopy and Nano-Imaging. *Science* **318**, 1750–1753 (2007).

25. Baum, P., Yang, D. S. & Zewail, A. H. 4D visualization of transitional structures in phase transformations by electron diffraction. *Science* **318**, 788–792 (2007).
26. Yuan, X., Zhang, W. & Zhang, P. Hole-lattice coupling and photoinduced insulator-metal transition in VO₂. *Physical Review B - Condensed Matter and Materials Physics* **88**, 035119 (2013).
27. Jellison, G. E. & Modine, F. A. Parameterization of the optical functions of amorphous materials in the interband region. *Applied Physics Letters* **69**, 371–373 (1996).
28. Johannsen, J. C. *et al.* Direct View of Hot Carrier Dynamics in Graphene. *Phys. Rev. Lett.* **111**, 027403 (2013).
29. Zhang, L. *et al.* Light-induced phase transitions in vanadium dioxide: a tensor network study. Preprint at <https://arxiv.org/abs/2402.01247>.
30. Xu, J., Chen, D. & Meng, S. Decoupled ultrafast electronic and structural phase transitions in photoexcited monoclinic VO₂. *Sci. Adv.* **8**, eadd2392 (2022).
31. Johnson, A. S. *et al.* All-optical seeding of a light-induced phase transition with correlated disorder. Preprint at <https://doi.org/10.48550/arXiv.2309.13275>.
32. Xu, S., Shen, X., Hallman, K. A., Haglund, R. F. & Pantelides, S. T. Unified band-theoretic description of structural, electronic, and magnetic properties of vanadium dioxide phases. *Phys. Rev. B* **95**, 125105 (2017).
33. Shao, Z., Cao, X., Luo, H. & Jin, P. Recent progress in the phase-transition mechanism and modulation of vanadium dioxide materials. *NPG Asia Materials* **10**, 581–605 (2018).
34. Giannetti, C. *et al.* Ultrafast optical spectroscopy of strongly correlated materials and high-temperature superconductors: a non-equilibrium approach. *Advances in Physics* **65**, 58–238 (2016).
35. Marvel, R. E., Harl, R. R., Craciun, V., Rogers, B. R. & Haglund, R. F. Influence of deposition process and substrate on the phase transition of vanadium dioxide thin films. *Acta Materialia* **91**, 217–226 (2015).
36. De Sousa Meneses, D., Malki, M. & Echegut, P. Structure and lattice dynamics of binary lead silicate glasses investigated by infrared spectroscopy. *Journal of Non-Crystalline Solids* **352**, 769–776 (2006).
37. Shao, C., Tohyama, T., Luo, H.-G. & Lu, H. Numerical method to compute optical conductivity based on pump-probe simulations. *Phys. Rev. B* **93**, 195144 (2016).
38. Kresse, G. & Joubert, D. From ultrasoft pseudopotentials to the projector augmented-wave method. *Phys. Rev. B* **59**, 1758–1775 (1999).
39. Kresse, G. & Furthmüller, J. Efficient iterative schemes for *ab initio* total-energy calculations using a plane-wave basis set. *Phys. Rev. B* **54**, 11169–11186 (1996).
40. Perdew, J. P., Ernzerhof, M. & Burke, K. Rationale for mixing exact exchange with density functional approximations. *The Journal of Chemical Physics* **105**, 9982–9985 (1996).
41. Adamo, C. & Barone, V. Toward reliable density functional methods without adjustable parameters: The PBE0 model. *The Journal of Chemical Physics* **110**, 6158–6170 (1999).

Acknowledgements

This work was funded by the European Research Council (ERC) under the European Union’s Horizon 2020 research and innovation programme: Starting Grant agreement HISOL no. 679649 and ERC Consolidator Grant XSOL no. 101001534. CB and JCT acknowledge support from the United Kingdom's Engineering and Physical Sciences Research Council: Grant agreement EP/T020903/1. CB acknowledges support from the Royal Academy of Engineering through Research Fellowship No. RF/202122/21/133.

This work was funded by the Spanish AIE (projects PID2022-137817NA-I00 and EUR2022-134052).

ASJ acknowledges the support of the Ramón y Cajal Program (Grant RYC2021-032392-I). IMDEA Nanociencia acknowledges support from the “Severo Ochoa” Programme for Centers of Excellence in R&D (MICIN, CEX2020-001039-S).

Computational resources were provided by the High-Performance Computing Center at the University of Memphis (X. S.)

U.B. is also grateful for the financial support of the IBM Quantum Researcher Program. R.W.C. acknowledges support from the Polish National Science Centre (NCN) under the Maestro Grant No. DEC-2019/34/A/ST2/00081.

T.G. acknowledges funding by Gipuzkoa Provincial Council (QUAN-000021-01), by the Department of Education of the Basque Government through the IKUR strategy and through the project PIBA_2023_1_0021 (TENINT), by the Agencia Estatal de Investigación (AEI) through Proyectos de Generación de Conocimiento PID2022-142308NA-I00 (EXQUSMI), by the BBVA Foundation (Beca Leonardo a Investigadores en Física 2023). The BBVA Foundation is not responsible for the opinions, comments and contents included in the project and/or the results derived therefrom, which are the total and absolute responsibility of the authors.

S.T.P. acknowledges funding from the U. S. Department of Energy, Office of Science, Basic Energy Sciences, Materials Science and Engineering Directorate grant No. DE-FG02-09ER46554 and by the McMinn Endowment at Vanderbilt University.

The ICFO group acknowledges support from:

ERC AdG NOQIA; MCIN/AEI (PGC2018-0910.13039/501100011033, CEX2019-000910-S/10.13039/501100011033, Plan National FIDEUA PID2019-106901GB-I00, Plan National STAMEENA PID2022-139099NB-I00 project funded by MCIN/AEI/10.13039/501100011033 and by the “European Union NextGenerationEU/PRTR” (PRTR-C17.I1), FPI); QUANTERA MAQS PCI2019-111828-2);

QUANTERA DYNAMITE PCI2022-132919 (QuantERA II Programme co-funded by European Union’s Horizon 2020 program under Grant Agreement No 101017733), Ministry of Economic Affairs and Digital Transformation of the Spanish Government through the QUANTUM ENIA project call – Quantum Spain project, and by the European Union through the Recovery, Transformation, and Resilience Plan – NextGenerationEU within the framework of the Digital Spain 2026 Agenda; Fundació Cellex; Fundació Mir-Puig; Generalitat de Catalunya (European Social Fund FEDER and CERCA program, AGAUR Grant No. 2021 SGR 01452, QuantumCAT \ U16-011424, co-funded by ERDF Operational Program of Catalonia 2014–2020); Barcelona Supercomputing Center MareNostrum (FI-2023-1-0013); EU Quantum Flagship (PASQuanS2.1, 101113690); EU Horizon 2020 FET-OPEN OPTologic (Grant No 899794); EU Horizon Europe Program (Grant Agreement 101080086 — NeQST), ICFO Internal “QuantumGaudi” project; European Union’s Horizon 2020 program under the Marie Skłodowska-Curie grant agreement No 847648; “La Caixa” Junior Leaders fellowships, “La Caixa” Foundation (ID 100010434): CF/BQ/PR23/11980043.

Views and opinions expressed are, however, those of the author(s) only and do not necessarily reflect those of the European Union, European Commission, European Climate, Infrastructure and Environment Executive Agency (CINEA), or any other granting authority. Neither the European Union nor any granting authority can be held responsible for them. JO would like to thank Tom Tiwald and Inga Potsch of J.A. Woollam Co. for fruitful discussions.

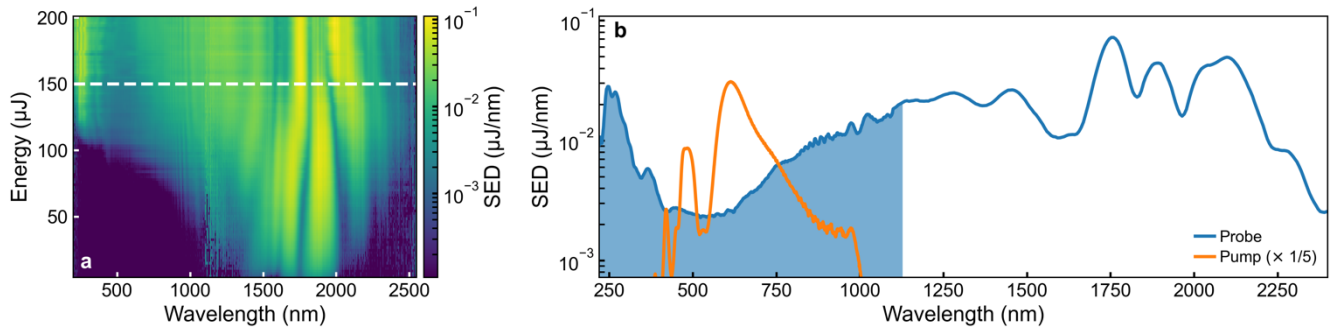
Author contributions

CB, JCT and ASJ conceived the study. RH and KH grew the VO₂ samples. CB and JCT designed the ultra-broadband few-femtosecond spectroscopy experiments, and CB constructed the apparatus and performed the experiments. MR, JO and ASJ performed additional characterization experiments. XS and STP developed the density functional theory model and XS did the calculations. LZ, UB, TG, RWC, ML and ASJ developed the TN-MF model, while LZ did the calculations. CB and ASJ analysed the data and wrote the paper with contributions from all authors.

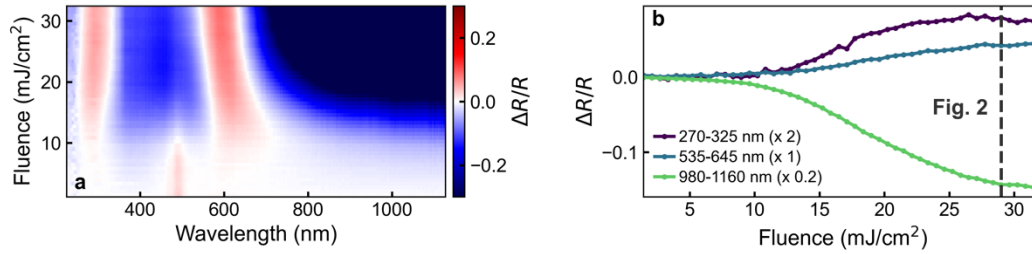
Competing interests

The authors declare no competing interests.

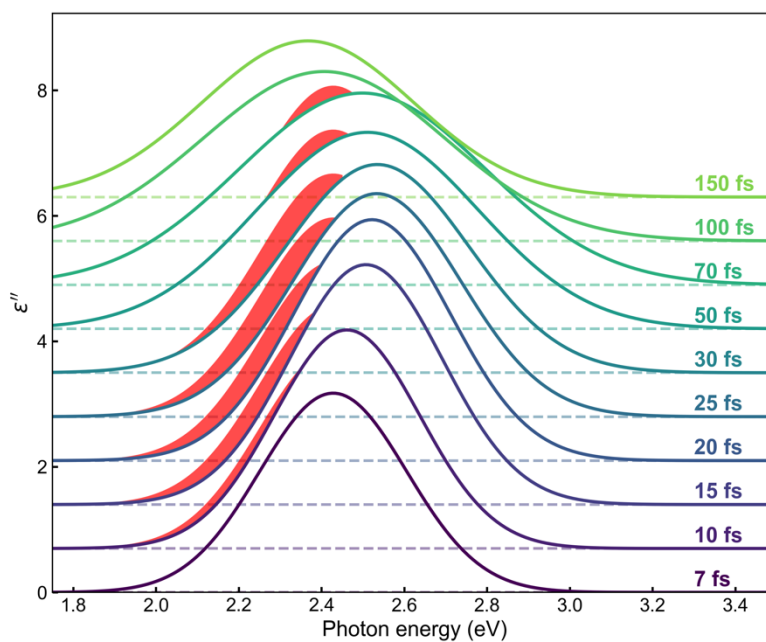
Extended Data



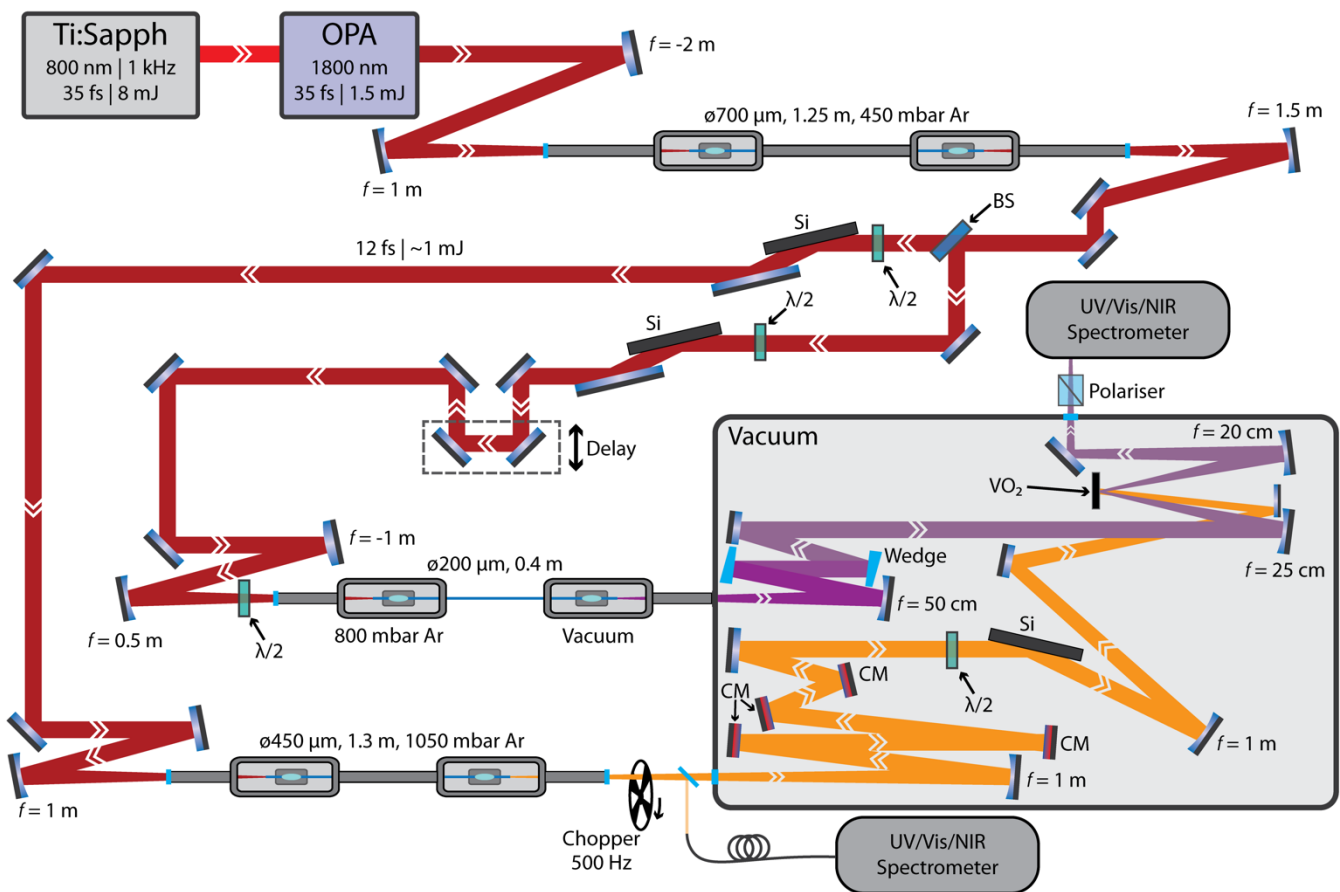
Extended Data Fig. S1: Pump and probe spectra. **a**, Energy-dependent output probe spectrum on a logarithmic colour scale. The white dashed line indicates the energy used in the experiments (150 μJ). **b**, Probe spectrum at 150 μJ (blue) and the spectrum of the pump pulse (orange). The shaded area indicates the spectral region covered in the pump-probe measurements in Fig. 2.



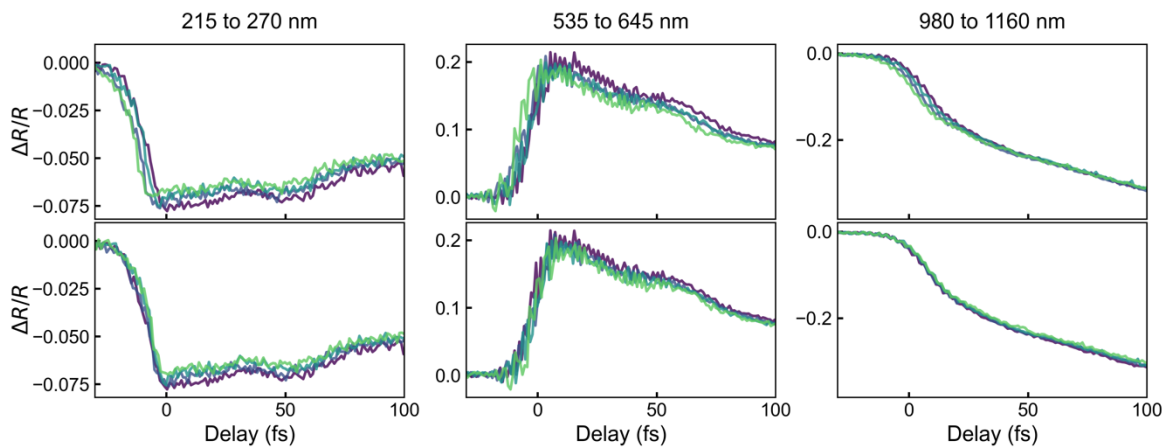
Extended Data Fig. S2: Fluence threshold for the IMT. **a**, Fluence-dependent differential reflectivity at a fixed pump-probe delay of 1 ps. The incident fluence is determined as $F = 4E/(\pi w_x w_y)$, where E is the on-target pulse energy and w_x and w_y are the FWHM focal spot widths in the x and y axes, respectively. The positive feature around 490 nm at low fluence is an artefact due to pump scatter. **b**, Lineouts of the data shown in **a** in three different wavelength bands, clearly showing the onset of the IMT around 10 mJ/cm^2 . The vertical dashed line indicates the fluence used for the pump-probe experiments shown in Fig. 2, which for the penetration length of the pump and our film thickness ensures excitation across the phase transition in the full depth of the VO_2 . At fluences below 10 mJ/cm^2 we see clear 6 THz coherent phonons modulating the entire spectrum while, as shown in Figure 2, no such signature is observed.



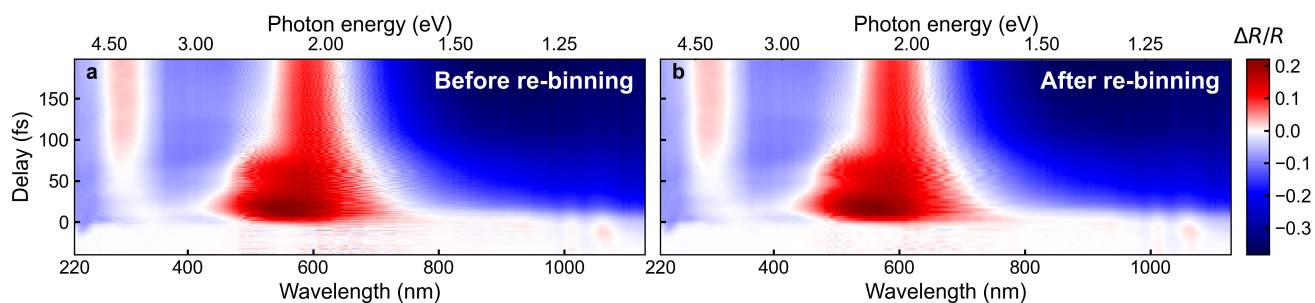
Extended Data Fig. S3: Shift in the d_{\parallel} transition and density-of-states bottleneck. Each line shows the imaginary part of the permittivity ϵ'' due to only the $O_{2p} \rightarrow d_{\parallel}$ transition at one delay. Compared to the state immediately after photoexcitation, the transition shifts around 0.2 eV higher in energy and the transition strength on the low-energy side is reduced (red shaded areas). This is clear evidence of a transient reduction in the density of states just above the Fermi level.



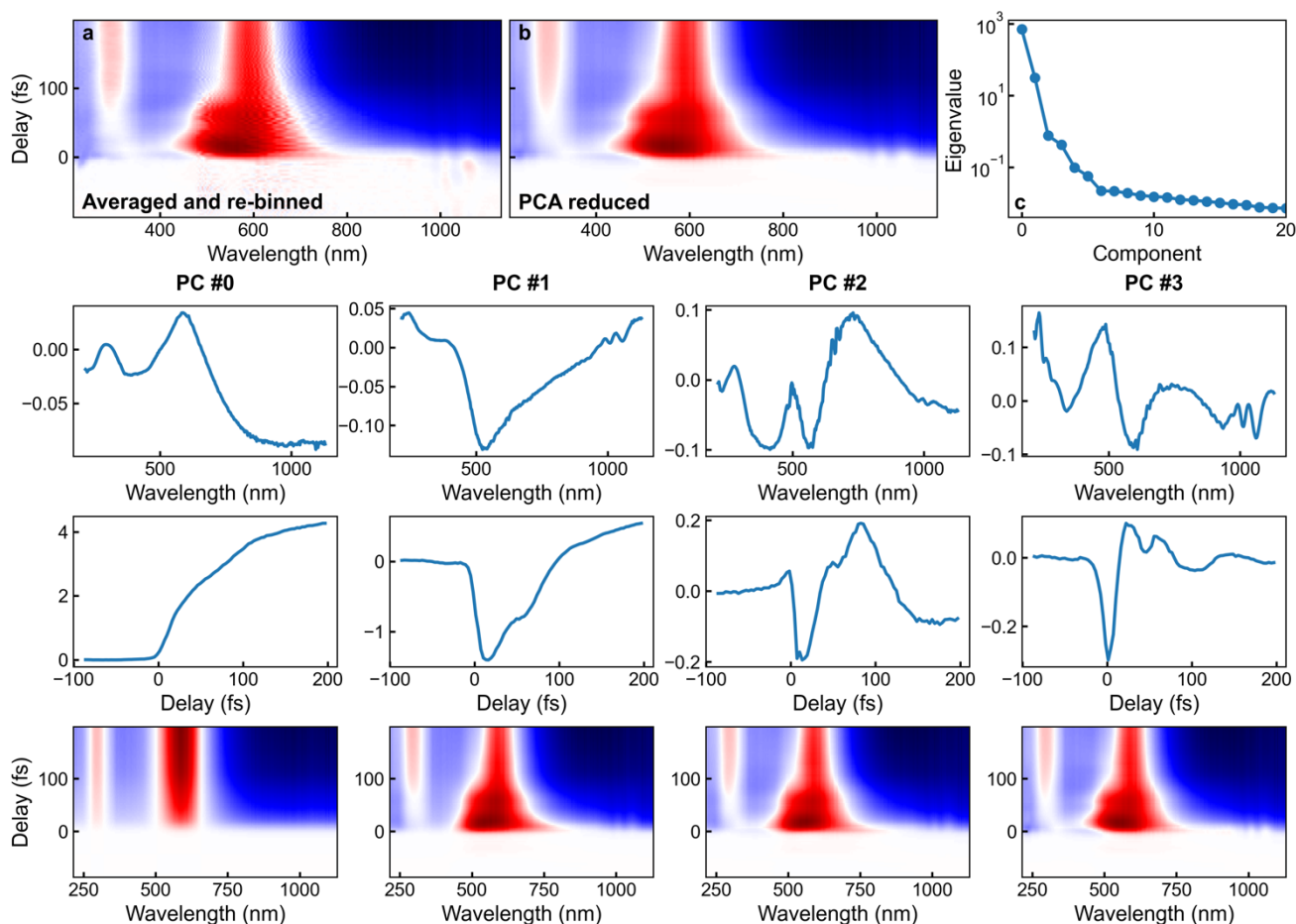
Extended Data Fig. S4: Layout of the experimental apparatus. 35 fs laser pulses at 800 nm are converted to 1800 nm wavelength in an optical parametric amplifier (OPA) and compressed to 12 fs duration in a first gas-filled hollow capillary fibre (HCF). After beamsplitting and attenuation, pump and probe pulses are generated in separate second-stage HCFs. Inside a vacuum chamber, pump and probe pulses are overlapped in space in time on a VO₂ sample. The reflected probe is analysed by a spectrometer outside the chamber. A second synchronised spectrometer measures the pump spectrum before the vacuum chamber and after a chopper wheel to reference the pump-on/pump-probe shots.



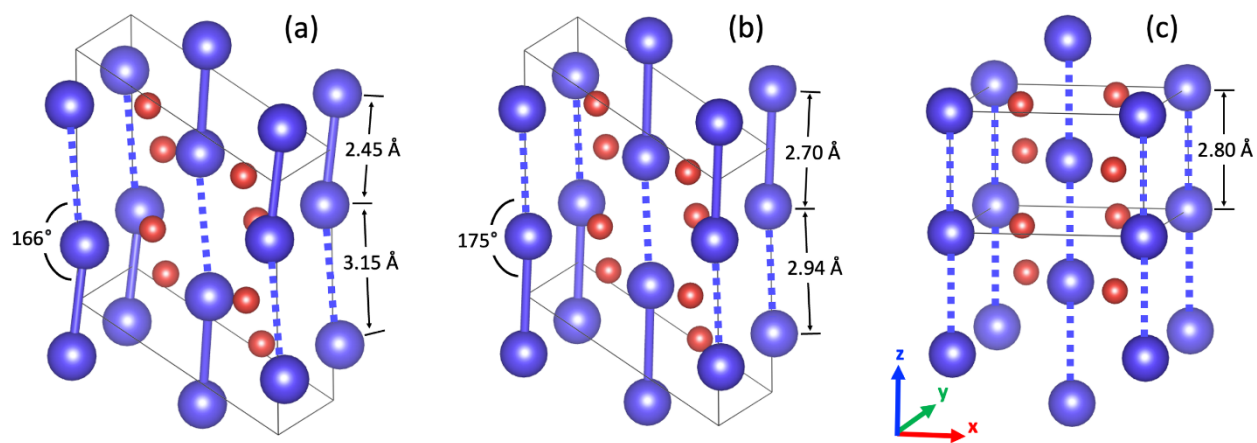
Extended Data Fig. S5: Delay axis correction. Each column shows one of the line-outs shown in Fig. 2b. Each line corresponds to one of the four subsequent delay scans in the experiment. The top row shows line-outs from the raw data and the bottom row shows line-outs from the delay-corrected data.



Extended Data Fig. S6: Delay-axis rebinning. **a**, Delay-corrected and averaged scans with full delay resolution (1 fs steps). **b**, The data in **a** after re-binning along the delay axis by a factor 3 to remove fast coherent artefacts.



Extended Data Fig. S7: Principal-component analysis. Top: differential reflectivity after re-binning (**a**) and after PCA reduction (**b**). Bottom: each column shows the wavelength-axis eigenvector (first row) and delay-axis eigenvector (second row) of one principal component. The bottom row shows the cumulative result of the PCA reconstruction, showing that with 4 components, all essential features of the data are reproduced.



Extended Data Fig. S8: The DFT calculated lattice structure of the M1 (a), M0 (b), and R (c) phases of VO₂. Shown are the relevant long and short vanadium-vanadium bond lengths as well as angles. Converted from bond lengths and angles into the X1 and X2 nomenclature used in the main text (deviations from the R phase positions), we obtain phase $X_1=0.187$ Å and $X_2=0.168$ Å in the M1 phase, $X_1=0.051$ Å and $X_2=0.061$ Å in the M0 phase, and $X_1=X_2=0$ in the R phase.